Elastic Relaxation of Fluid-Driven Cracks and the Resulting Backflow

Ching-Yao Lai,[1] Zhong Zheng,[1,2] Emilie Dressaire,[3] Guy Z. Ramon,[4] Herbert E. Huppert,[2,5] and Howard A. Stone[1,*]

[1]*Department of Mechanical and Aerospace Engineering, Princeton University, Princeton, New Jersey 08544, USA*
[2]*Institute of Theoretical Geophysics, Department of Applied Mathematics and Theoretical Physics,*
University of Cambridge, Cambridge CB3 0WA, United Kingdom
[3]*Department of Mechanical and Aerospace Engineering, New York University Tandon School of Engineering,*
Brooklyn, New York 11201, USA
[4]*Department of Civil and Environmental Engineering, Technion–Israel Institute of Technology, Haifa 32000, Israel*
[5]*School of Mathematics and Statistics, University of New South Wales, Sydney, New South Wales 2052, Australia*
(Received 30 September 2016; published 23 December 2016)

Cracks filled with fluid propagation when the pressurized fluid is injected into the crack. Subsequently, when the fluid inlet is exposed to a lower pressure, the fluid flows backwards (backflow) and the crack closes due to the elastic relaxation of the solid. Here we study the dynamics of the crack closure during the backflow. We find that the crack radius remains constant and the fluid volume in the crack decreases with time in a power-law manner at late times. The balance between the viscous stresses in the fluid and elastic stresses in the fluid and the elastic stresses in the solid yields a scaling law that agrees with the experimental results for different fluid viscosities, Young's moduli of the solid, and initial radii of the cracks. Furthermore, we visualize the time-dependent crack shapes, and the convergence to a universal dimensionless shape demonstrates the self-similarity of the crack shapes during the backflow process.

The interplay of fluids and cracks is ubiquitous in nature and industry, and includes dynamics such as magma intrusion into Earth's crust [1,2], cracks opening at cell-cell contacts [3,4], and hydraulic fracturing of shale formations for oil and gas extraction [5,6]. The injection of pressurized fluid into cracks in a brittle solid causes crack propagation (fluid-driven cracks), and has been previously investigated [6–10]. However, the closure of fluid-filled cracks due to elastic relaxation has not been systematically studied. For example, this topic is closely related to the environmental issue of flowback in hydraulic fracturing and also arises in the trapping of fluids due to geophysical processes involving release of elastic stresses.

In this Letter, we study the dynamics of the elastic relaxation of a liquid-filled crack, once an outlet at the center of the crack is exposed to atmospheric pressure [Fig. 1(a)]. The resulting pressure gradient within the crack causes the fluid to drain out through the outlet. This setup serves as a laboratory-scale model of practical flowback processes in industrial oil and gas extraction from hydro-fractured reservoirs. For the model material that we use here, i.e. gelatin, we report that the shapes of the crack during closure are self-similar and our experimental measurements agree with our scaling arguments at late times.

To study the effect of different experimental parameters, we changed the gelatin Young's modulus E by varying the concentration of gelatin powder (gelatin type A, ThermoFisher Scientific, U.S.) in tap water. The mixture of water and gelatin powder was then refrigerated for approximately 10 h and solidified so as to be ready for the experiments. Young's moduli E ranging from 66 ± 6.6

to 104 ± 10.4 kPa, as measured via indentation tests [11], were used in our experiments. Mineral oils (Sigma-Aldrich, U.S.) with viscosities $\mu = 11.5 \pm 0.2$ and 26.9 ± 0.1 mPa s, and a polymeric fluid (VeroBlue RGD840, Stratasys, U.S.) with viscosity $\mu = 149 \pm 3.2$ mPa s, as measured with a rheometer (Physica MCR 301), were used to generate the liquid-filled crack in the gelatin. Both the mineral oils and the polymeric fluid we used were Newtonian at the typical shear rates of the experiments. Note that water is miscible with gelatin at the time scale of the experiments and hence would not be a proper choice of liquid for our experiments.

We conducted a series of experiments to first generate a fluid-driven crack [9,10]. Then, we measured the liquid volume remaining in the crack as a function of time as the stress in the system relaxes. In the setup, a long tube of inner radius 1.59 mm filled with a liquid (dyed red) is connected to a needle with inner radius 1.08 mm. The needle is inserted into a tank of solid gelatin (width × length × height = 150 mm × 150 mm × 113 mm), as shown schematically in Fig. 1. A disk-shaped liquid-filled crack is generated in the gelatin, in a plane perpendicular to the tip of the needle due to the pressure increase from liquid injection through the tube [9]. We can control the crack radius, the fluid viscosity, and the elasticity of the matrix.

After the tube is exposed to the atmospheric pressure, the liquid flows back towards the open end of the tube, which we refer to as backflow [see Fig. 1(c)], and the liquid-filled crack slowly closes due to the elastic relaxation of the solid gelatin [see Fig. 1(b)]. A USB camera (1280 × 1024 pixels, frame rate = 10 fps) is placed above the experimental system to record the shape evolution of
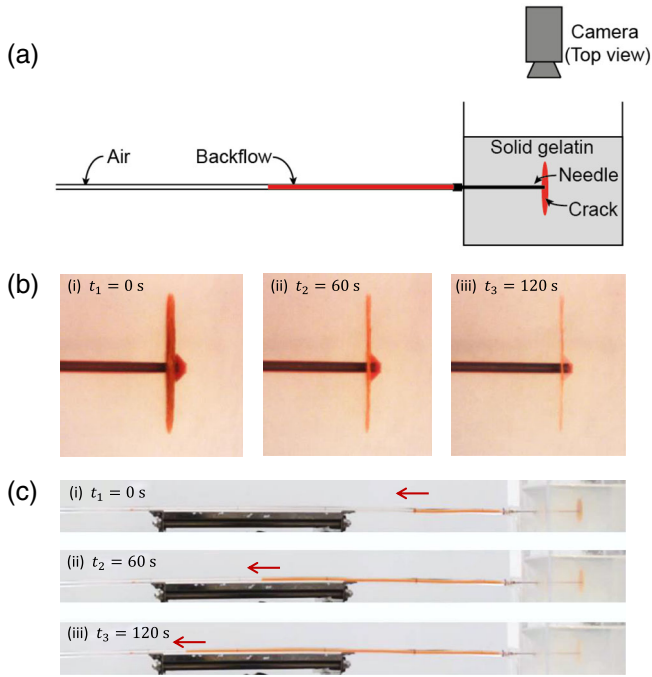
FIG. 1.   (a) Schematic of the experimental setup. Representative experimental views from the (b) top and (c) side are shown. Experimental parameters: mineral oil (dye in red) viscosity $\mu = 26.9$ mPa s, gelatin Young's modulus $E = 79$ kPa, and the initial crack radius $R = 21$ mm. (b) The shape of the liquid-filled crack at different times as the elastic solid relaxes. (c) The propagation of liquid (dyed red) from the crack toward the open end of the tube (backflow), with the red arrows above the liquid fronts indicating the flow direction.

the crack, and a Nikon D7100 camera (1920×1080 pixels, frame rate $= 24$ fps) is placed on the side to record the backflow dynamics.

An important observation for the backflow experiments is that when the liquid-filled crack closes, only the thickness of the crack decreases, as the radius R of the crack remains nearly unchanged, as evident in Fig. 1(b). Note that in other parameter regimes a decrease in crack radius during crack closure has been reported in gels [12].

The liquid volume in the crack V at different times can be calculated by subtracting the fluid volume in the tube from the total amount of liquid injected into the gelatin. The results vary significantly when either E or μ changes. Representative results for $V(t)$ with different experimental parameters are shown in Fig. 3(a), which will be discussed shortly.

To understand how the elastic relaxation of a liquid-filled crack causes the liquid to drain out of the crack, we use scaling arguments. We consider the model of an axisymmetric fluid-driven crack confined in an infinite elastic medium, which is commonly modeled as a penny-shaped crack [7–9], as shown schematically in Fig. 2. The geometry of the crack sets the typical elastic pressure $P(t)$,
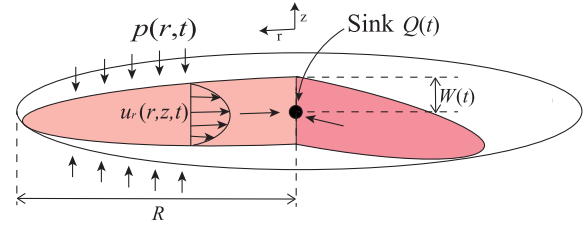

FIG. 2.   Schematic of the fluid flow in a crack of radius R and half maximum thickness $W(t)$ in an elastic reservoir during the backflow process. The elastic pressure $p(r, t)$ surrounding the crack drives the fluid to flow towards the center and drain out of the crack with a volumetric flow rate $Q(t)$.

$$P \approx \frac{W}{R} \frac{E}{2(1 - \nu^2)}, \tag{1}$$

where ν is Poisson's ratio, and R and W are, respectively, the crack radius and maximum half crack thickness. At the crack surface the fluid pressure is the same as the local elastic pressure $p(r, t)$. In a narrow crack where $W \ll R$, the lubrication approximation is applicable for the fluid flow and the fluid pressure is assumed to only vary along the crack. The radial pressure gradient drives the fluid to flow inward radially, with a parabolic velocity profile $u_r(r, z, t) = (1/2\mu)(\partial p/\partial r)[w(r, t)^2 - z^2]$, where $w(r, t)$ is the crack half thickness. Combining the continuity equation with the velocity profile integrated between the crack surfaces, we find the time rate of change of the crack thickness to be the order of magnitude

$$\frac{W}{t} \approx \frac{1}{3\mu} \frac{W^3 P}{R^2}. \tag{2}$$

The liquid volume in the crack is estimated as

$$V \approx 4\pi R^2 W. \tag{3}$$

Combining Eqs. (1)–(3) and assuming R is constant (consistent with the experiments), we obtain

$$\frac{V}{R^3} \approx \left(\frac{t}{T}\right)^{-1/3}, \tag{4}$$

where the time scale T is defined as

$$T \equiv \frac{384\pi^3 \mu (1 - \nu^2)}{E}. \tag{5}$$

The scaling arguments predict that the liquid volume in the crack decays with time according to $t^{-1/3}$.

After rescaling the experimental data for V and t in Fig. 3(a) using R and T, respectively, the data for different E, μ, and R collapse, as shown in Fig. 3(b). Also, V at late times exhibits a $t^{-1/3}$ dependence, which is consistent with
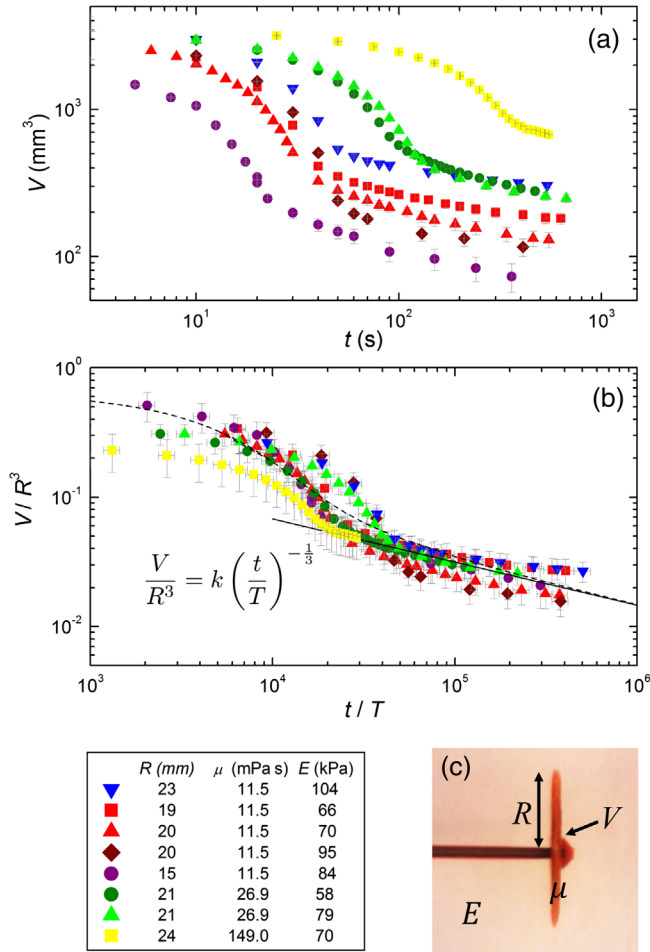
FIG. 3.   (a) The dependence of the liquid volume in the crack V on time t for different liquid viscosities μ, Young's moduli E, and crack radii R. (b) The dimensionless liquid volume in the crack versus time rescaled with R^3 and T, respectively, based on Eqs. (4) and (5). The error bars are estimated according to the measurement uncertainties. The $t^{-1/3}$ power law at late times is shown as the dark line with a prefactor $k = 1.46$ for Eq. (4) from fitting all data at late times. The dashed curve is the solution to Eq. (6) fitted to the purple circles ($A \approx 1$ and $B \approx 1206$ calculated using $R = 15$ mm), with $\alpha = 5$, $\beta = 0.03$ (see Supplemental Material [13]). (c) Definitions of the parameters.

our scaling law. The prefactor $k = 1.46$ for the $t^{-1/3}$ power law in Eq. (4), shown as the dark line in Fig. 3(b), is found by fitting all experimental data at the late times. The error bars in Fig. 3 are estimated based on the measurement uncertainties, such as the Young's modulus of the solid gelatin E (± 10 kPa), the liquid viscosity μ (± 3.2 mPa s), the crack radius R (± 2.6 mm), the liquid volume in the crack V (± 16 mm³), and time t (± 0.042 s).

To check our assumptions, we estimate the effective Reynolds number Re$_{\mathrm{eff}}$ of the fluid flow in the crack, and the viscous resistance in the tube and the needle compared with that in the crack. For a liquid of density $\rho \approx 850$ kg/m³ and viscosity $\mu = 26.9$ mPa s, a crack of typical

radius $R \approx 20$ mm, half thickness $W \approx 0.04$ mm, and a typical time scale halfway through an experiment $t \approx 100$ s, the effective Reynolds number in the crack is Re$_{\mathrm{eff}} \approx \rho u_r W^2 \mu^{-1} R^{-1} \approx \rho W^2 \mu^{-1} t^{-1} \approx 5 \times 10^{-7}$. Thus, the lubrication approximation applies and the inertial effects are negligible. The typical viscous stresses in the crack are estimated to be $\mu R^2 W^{-2} t^{-1} \approx 67$ Pa, whereas the viscous stresses in the long tube are $\mu U L a^{-2} \approx 0.6$ Pa, for a typical velocity $U \approx 10^{-4}$ m/s, length of liquid $L \approx 0.58$ m in the tube, and the inner radius of the tube $a \approx 1.59$ mm. Similarly, midway through the experiments the viscous stresses in the needle are estimated to be 0.4 Pa. Since the viscous stresses in the tube and the needle are much smaller than the typical stresses in the crack, we only consider the viscous resistance in the crack in our scaling arguments for the late-time dynamics. Next, we discuss the importance of these channel flow effects at early times.

We have shown that at late times the volume of the crack V exhibits a power-law dependence with time. At early times, however, the backflow dynamics does not obey Eq. (4), as shown in Fig. 3(b). It can be shown (see Supplemental Material [13]) that the viscous pressure drop in the tube and the needle ΔP_t at early times is not negligible compared to the viscous pressure drop in the crack ΔP_c. Thus, we developed a model of pressure drops in series, which are balanced by the elastic pressure $P(t)$, $\Delta P_t(t) + \Delta P_c(t) = P(t)$. The pressure drop along the flow path is linked to flow speed by the Poiseuille law. Carrying out these steps and using volume conservation, we obtain an ordinary differential equation, which in dimensionless form can be written as (see Supplemental Material [13])

$$\frac{d\hat{V}}{d\hat{t}}\left(\frac{B(\hat{V}_0 - \hat{V} + A)}{\hat{V}} + \frac{\alpha^3 \beta}{2\hat{V}^4}\right) + \frac{1}{\alpha} = 0, \qquad (6)$$

where $\hat{V} \equiv V/R^3$ and $\hat{t} \equiv t/T$ are, respectively, the dimensionless crack volume and time introduced earlier [see Eqs. (4) and (5)]; $B \equiv (R/a)^6/6\pi^4$, where a is the radius of the tube. The constant A is dependent on R, a, and the radius and length of the needle. Also, $\hat{V}_0 \equiv \hat{V}(t = 0)$ and α and β are fitting parameters (dimensionless). The term $B(\hat{V}_0 - \hat{V} + A)/\hat{V}$ in Eq. (6) arises from the viscous resistance from the tube and needle, whereas the $\alpha^3 \beta/2\hat{V}^4$ term comes from the viscous resistance in the crack, which dominates at late times and results in the $t^{-1/3}$ scaling law consistent with Eq. (4). The numerical solutions to Eq. (6) for different A and B depend on R at early times but approach a universal (R-independent) solution at late times (see Supplemental Material for details [13]). The agreement between the solution to Eq. (6) and the experiment of $R = 15$ mm is shown in Fig. 3(b) by the dashed curve ($A \approx 1$ and $B \approx 1206$).

In addition, we developed an imaging technique to visualize the shape of the crack as a function of time.
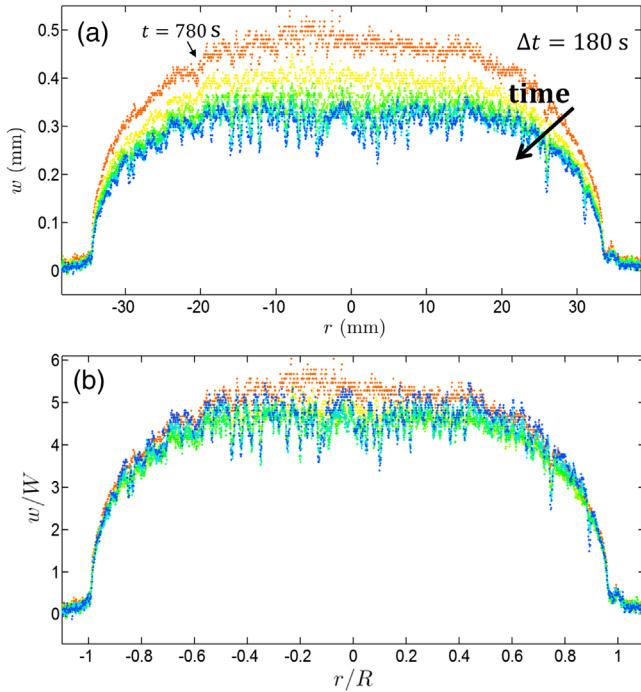
FIG. 4.   (a) Time evolution of the half crack thickness profile $w(r, t)$, measured along a fixed cross section of a crack. $\Delta t = 180$ s represents the time difference between curves of different colors. Experimental parameters in this experiment are $\mu = 149$ mPa s, $E = 55$ kPa, $R = 35$ mm. (b) Dimensionless profile of half crack thickness $w(r, t)$, rescaled based on Eq. (7). The collapse of the dimensionless crack profiles shows a good agreement between the scaling law and the experimental results at late times.

We set a light-emitting diode panel with a peak wavelength at 525 mm parallel to the surface of the crack filled with fluorescent dye, and then measured the fluorescent light intensity to determine the crack thickness $w(r, t)$ based on a separate calibration experiment. In Fig. 4, the polymeric fluid in the crack is mixed with Nile red (Sigma-Aldrich), which absorbs green light and emits red light (the concentration of the mixture is 30 μg Nile red per mL liquid). A Nikon D5100 camera (4928×3264 pixels) attached to a long pass filter (O-54 (540 nm), Edmund Optics, U.S.) was used to record the light intensity distribution of the crack. The thicker the dye-filled crack, the stronger the fluorescent light intensity captured by the camera. A UV protection film was used to prevent UV light from the light-emitting diode changing the rheology of the polymeric fluid. Also, during the image analysis, we only use information from the red channel. We can thus calibrate the light intensity (only due to the fluorescence) with the thickness of the crack.

The time evolution of the crack profile is shown in Fig. 4(a). The crack thickness was measured across a fixed cross section every 180 s. We assume the crack to be axisymmetric with respect to the z axis and divide the measured crack thickness by a factor of 2 to get $w(r, t)$, the

half crack thickness profile. Data points of the same color were taken at the same time.

To nondimensionalize the crack profiles $w(r, t)$, we obtain a scaling law for the typical crack thickness W using Eqs. (3) and (4):

$$W \approx \frac{R}{4\pi} \left(\frac{t}{T} \right)^{-1/3}, \qquad (7)$$

where T is defined in Eq. (5), and R is the constant radius during backflow. After we rescale the crack profiles in Fig. 4(a), we obtain a collapse of the dimensionless crack profiles at the late times, as shown in Fig. 4(b). The collapse of the dimensionless liquid volume $V(t)$ in Fig. 3(b) and the dimensionless $w(r, t)$ at the late times in Fig. 4(b) show that the crack profiles are self-similar and the data at the late times agree with our scaling arguments.

In summary, we studied the dynamics of the elastic relaxation of a fluid-driven crack during the crack closure. In our experiments we observed that the crack radius remains a constant during the closure process. The experiments show that the fluid volume V in the crack decays with time as $t^{-1/3}$ at late times, and is affected by the viscosity of fluid in the crack μ, elasticity of the solid E, and the crack radius R. We also reported the time evolution of the crack shapes $w(r, t)$ and the universal dimensionless crack shapes. At late times, the results agree with the scaling arguments balancing the viscous stresses in the fluid flow along the crack and the elastic stresses applied on the crack surfaces. At early times, the result can be explained by the non-negligible viscous resistance in the outlet channels. While numerous studies focused on the propagation of fluid-driven cracks, we examined the backflow dynamics caused by the elastic relaxation and the closure of the crack. Our results may relate to environmental issues such as the pollution of the water flowing back from the wells in hydraulic fracturing and other subsurface engineering and geophysical processes.

*hastone@princeton.edu
[1] A. M. Rubin, Annu. Rev. Earth Planet Sci. **23**, 287 (1995).
[2] J. R. Lister and R. C. Kerr, J. Geophys. Res. **96**, 10049 (1991).

[3] L. Casares, R. Vincent, D. Zalvidea, N. Campillo, D. Navajas, M. Arroyo, and X. Trepat, Nat. Mater. **14**, 343 (2015).

[4] A. Lucantonio, G. Noselli, X. Trepat, A. DeSimone, and M. Arroyo, Phys. Rev. Lett. **115**, 188105 (2015).

[5] S. A. Khristianovic and Y. P. Zheltov, *Proceedings of 4th World Petroleum Congress, Rome, Italy* (Carlo Colombo Publishers, 1955), 576, Vol. 2.

[6] E. Detournay, Annu. Rev. Fluid Mech. **48**, 311 (2016).

[7] A. Spence and P. Sharp, Proc. R. Soc. A **400**, 289 (1985).

[8] A. A. Savitski and E. Detournay, Int. J. Solids Struct. **39**, 6311 (2002).

[9] C. Y. Lai, Z. Zheng, E. Dressaire, J. S. Wexler, and H. A. Stone, Proc. R. Soc. A **471**, 20150255 (2015).

[10] C. Y. Lai, Z. Zheng, E. Dressaire, and H. A. Stone, Phil. Trans. R. Soc. A **374**, 20150425 (2016).

[11] R. Long, M. S. Hall, M. Wu, and C. Y. Hui, Biophys. J. **101**, 643 (2011).

[12] F. Renard, D. K. Dysthe, J. G. Feder, P. Meakin, S. J. S. Morris, and B. Jamtveit, Geofluids **9**, 365 (2009).

[13] See Supplemental Material at http://link.aps.org/supplemental/10.1103/PhysRevLett.117.268001 for the derivation of the nonlinear ordinary differential equation [Eqs. (6)].